Reversible phase transition induced large piezoelectric response in Sm-doped $BiFeO_3$ with a composition near the morphotropic phase boundary

Zhenyu Liao,[1] Fei Xue,[2] Wei Sun,[3] Dongsheng Song,[1] Qiqi Zhang,[1] Jing-Feng Li,[3] Long-Qing Chen,[2] and Jing Zhu[1,*]

[1]*National Center for Electron Microscopy in Beijing, State Key Laboratory of New Ceramics and Fine Processing, Key Laboratory of Advanced Materials (MOE), School of Materials Science and Engineering, Tsinghua University, Beijing 100084, People's Republic of China*

[2]*Department of Materials Science and Engineering, The Pennsylvania State University, University Park, Pennsylvania 16802, USA*

[3]*State Key Laboratory of New Ceramics and Fine Processing, School of Materials Science and Engineering, Tsinghua University, Beijing 100084, People's Republic of China*

(Received 20 January 2017; revised manuscript received 27 April 2017; published 1 June 2017)

Materials with the morphotropic phase boundary (MPB) exhibit an ultrahigh mechanical response to electrical inputs, which has been widely used in applications such as sensors and actuators. Recently, the rare-earth element doped $BiFeO_3$ (BFO) was found to possess a MPB between a rhombohedral polar phase and an orthorhombic antipolar phase with enhanced piezoelectric response, enabling it to be an attractive alternative to toxic Pb-based piezoelectric materials. Despite theoretical and experimental efforts, the phase transition behavior under electric fields has not been directly confirmed, leaving a gap in the understanding of the origin of enhanced piezoelectricity. Here, we have demonstrated an irreversible electric-field induced phase transition from the antipolar phase to the polar phase in Sm-doped BFO with the pre-MPB composition, and a reversible phase transition between the polar phase and the antipolar/nonpolar phase in Sm-doped BFO with the MPB composition. *In situ* transmission electron microscopy technique combined with thermodynamic calculation based on the Ginzburg-Landau-Devonshire theory indicates that the electric-field induced reversible phase transition leads to enhanced piezoelectric response and double P-E hysteresis loops. These results provide us a deep insight into the mechanism of exotic electromechanical response in the rare-earth element doped BFO system with the composition near the MPB.

DOI: 10.1103/PhysRevB.95.214101

I. INTRODUCTION

A phase boundary, where two or three phases coexist with nearly degenerate free energies, plays an essential role in determining materials' properties. A material in the vicinity of the phase boundary usually exhibits significant physical responses in reaction to relatively weak external stimulus, such as electric fields, magnetic fields, and temperature. In the case of piezoelectric materials, ultralarge piezoelectric coefficients can be achieved in materials near the morphotropic phase boundary (MPB), dominated by lead-based ferroelectrics [1–4] such as $Pb(Zr_xTi_{1-x})O_3$ (PZT) and $Pb(Mg_{0.33}Nb_{0.67})O_3$-$PbTiO_3$ (PMN-PT), which play an essential role in a variety of applications ranging from ultrasonic imaging in the medical field to sonar in the national defense field. However, the application of lead has been strictly limited by antilead poisoning legislations owing to its toxicity, which stimulates a search for environment-friendly lead-free alternatives both in academic and industrial fields [5,6].

$BiFeO_3$ (BFO) has attracted broad attention as the only single-phase multiferroic material at room temperature discovered so far. It exhibits rhombohedral symmetry characterized by the $a^-a^-a^-$ octahedral tilting and cation displacement at room temperature (space group $R3c$). BFO possesses a very high Curie transition temperature ($Tc \sim 1103$ K) and high remnant polarization ($Pr \sim 100\,\mu C/cm^2$) [7]. The strong intrinsic coupling between the polarization and strain in BFO ensures potential applications in actuators and sensors. For instance, the coexistence of R and T phases with a remarkable enhancement of piezoresponse can be achieved in BFO grown on a compressive $LaAlO_3$ substrate [8], enabling it to be a promising substitution for its lead-based counterpart. Recent studies have revealed a ferroelectric to nonferroelectric MPB in A-site rare-earth element substituted BFO. In 2008, Fujino *et al.* reported a rhombohedra-orthorhombic (R-O) phase boundary with a high piezoelectric coefficient ($d_{33} \sim 110$ pm/V) in 14 at. % Sm-doped BFO [9]. Further transmission electron microscopy (TEM) investigation revealed that three major phases coexist in the MPB of Sm-doped BFO: R3c phase, $PbZrO_3$-like phase, and *Pnma* phase [10]. Due to the dramatically enhanced electromechanical properties including the piezoelectric coefficient d_{33} and the dielectric constant ε_{33} near the MPB, many studies have been devoted to rare-earth modified BFO in various forms, including single-crystal thin films [10–13], polycrystalline thin films [14,15], and ceramics [16,17]. It is widely accepted that the MPB is a universal phenomenon in $BiFeO_3$ doped with rare-earth elements (i.e., Sm, Gd, and Dy),which shows an onset of double hysteresis loop and large piezoelectric response. Despite some theoretical efforts [12,18], the essential issue, namely, the underlying mechanism of the enhancement of the piezoelectric coefficient, has not been clarified clearly by direct microscopic evidences in this field. To reveal this, it is imperative to understand the behavior of each phase in A-site doped BFO under external field.

Here, we took Sm-doped BFO as a model system to study the microscopic mechanism for the enhanced piezoelectric coefficient at the lead-free MPB. A full evolution of different phases in the system during the switching of external electric field was achieved by *in situ* structural characterization by TEM. Compared with routine methods, *in situ* TEM technique can provide information about the

*jzhu@mail.tsinghua.edu.cn

temporal evolution, enabling us to observe the phase transition behaviors in real time during switching through the thickness of the films. Our observations show the direct evidence of an irreversible phase transition from the antipolar phase to the polar phase in the sample with 12 at. % Sm-doping content (pre-MPB composition). For the sample with 14 at. % Sm-doping content (MPB composition), the transition is reversible between the antipolar/nonpolar phase and the polar phase. Combined with thermodynamic calculation based on Ginzburg-Landau-Devonshire theory, our results illustrate the microscopic origin of double hysteresis loops observed in macroscopic measurement, filling the gap of understanding the mechanism underlying the superior piezoelectric property in the A-site rare-earth element doped BFO with the composition near the MPB.

II. EXPERIMENTAL DETAILS

A-site Sm-doped BFO thin films were grown on closely lattice matched single-crystal (001) Nb-doped $SrTiO_3$ (Nb:STO) substrates by sol-gel method (refer to Ref. [19] for details). At room temperature, the composition of the MPB in these thin films is located at 14 at. % Sm-doping content where three phases coexist, consistent with the results in previous studies [9,10,12] despite radically different synthetic methods. The piezoelectric responses were characterized using an atomic force microscope (MFP-3D, Asylum Research, USA) with a functionality of piezoresponse force microscope for switching spectroscopy. A Pt/Ir-coated Arrow EFM cantilever (Nanoworld, USA, nominal spring constant 2.8 N/m, resonant frequency 75 kHz) was used.

Cross-sectional TEM specimens were prepared by conventional mechanical polishing followed by argon ion milling (Precision Ion Polishing System, Gatan). TEM characterization was carried out using FEI G20. *In situ* TEM experiments were carried out on a Nanofactory scanning tunneling microscopy system for TEM JEOL 2010F. For electrical switching, a bias voltage was applied between an electrochemically etched tungsten tip, used as a movable electrode, and the conductive 0.7 wt. % Nb-doped STO substrate which was electrically connected to the holder ground by silver paint. External electric field was applied using direct current voltages. In our *in situ* experiment, we change the electric bias manually with 0.5 V/step. At each step of applied voltage, we were waiting for the equilibrium state of the phase evolution. The time scale of each step is usually 5 s. The evolution of phase structure was imaged in real time with high resolution. The movies were recorded by a television-rate camera (Gatan) at 30 frames per second in JEOL 2010F.

The Sm-doped BFO system is phenomenologically described by two sets of order parameters, i.e., ferroelectric polarization $P_i (i = 1-3)$ and antiferroelectric order parameter $q_i (i = 1-3)$ [20]. The total free-energy polynomial functions are expanded to sixth order to include the characteristics of the first-order phase transition according to the Ginzburg-Landau-Devonshire theory, and it is written as

$$\begin{aligned} G = {} & a_{ij} P_i P_j + a_{ijkl} P_i P_j P_k P_l + a_{ijklmn} P_i P_j P_k P_l P_m P_n \\ & + b_{ij} q_i q_j + b_{ijkl} q_i q_j q_k q_l + b_{ijklmn} q_i q_j q_k q_l q_m q_n \\ & + t_{ijkl} P_i P_j q_k q_l, \end{aligned} \quad (1)$$

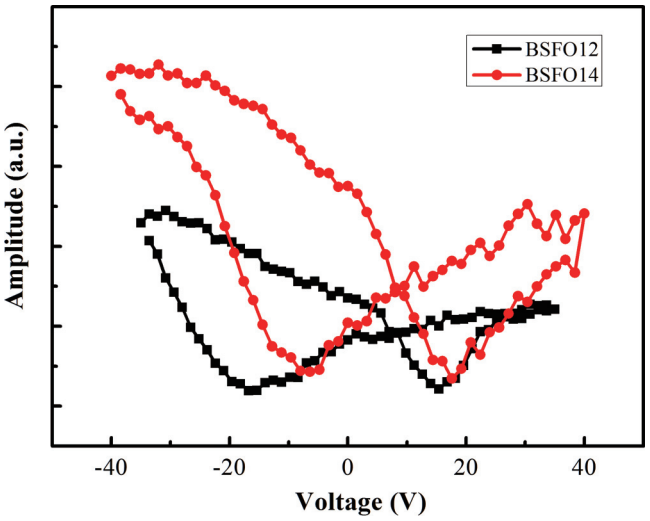

FIG. 1. The piezoelectric response of the sample BSFO12 (black curve) and BSFO14 (red curve), showing an enhanced piezoelectric response in BSFO14.

where a_{ij}, a_{ijkl}, and a_{ijklmn} are the ferroelectric dielectric stiffness; b_{ij}, b_{ijkl}, and b_{ijklmn} are the antiferroelectric dielectric stiffness; and t_{ijkl} are coupling coefficients between the polarization and antiferroelectric order parameters. For the coupling coefficients we take $t_{1111} = t_{1122} = 1.318 \times 10^8\ \mathrm{C^{-4}\,m^6\,N}$, and $t_{1212} = 0$, and all the other coefficients are listed in Ref. [20]. To calculate the energy landscape, we change the values of P_1 and P_2, and optimize the values of P_3, q_1, q_2, and q_3 to minimize the total free-energy density.

III. EXPERIMENTAL RESULTS AND DISCUSSIONS

Here, we focus on two types of samples with different Sm-doping contents: 12 at. % in the pre-MPB region (BSFO12) and 14 at. % in the MPB region (BSFO14). The piezoelectric responses of BSFO12 and BSFO14 were characterized by local switching spectroscopy piezoresponse force microscopy (SS-PFM) technique [21,22]. Details of the SS-PFM mode can be found elsewhere [23]. The piezoelectric responses manifest butterfly loops as shown in Fig. 1. The figure shows that BSFO14 possesses a much larger piezoelectric response than that of BSFO12, which is in agreement with previous studies [9,10,17].

A. Phase distribution in the BSFO12 sample (pre-MPB)

As shown in Fig. 2(a), the as-grown BSFO12 sample shows some nanoscale regions (outlined by white curves) with a distinct commensurate structural modulation along the $[011]_c$ direction. The fringe spacing along $[011]_c$ direction in these nanoscale regions is 1.13 nm, which is quadruple the spacing of the (011) lattice plane of the pseudocubic structure. As shown in Fig. 2(b), the $[100]_c$ zone axis diffraction pattern acquired from the region that includes both the matrix and the outlined nanoregion exhibits $\frac{1}{4}\{011\}$ superlattice reflections in addition to fundamental reflections. The electron-diffraction data along the $[010]_c$ zone axis [Fig. 2(c)] reveals additional $\frac{1}{4}\{100\}$

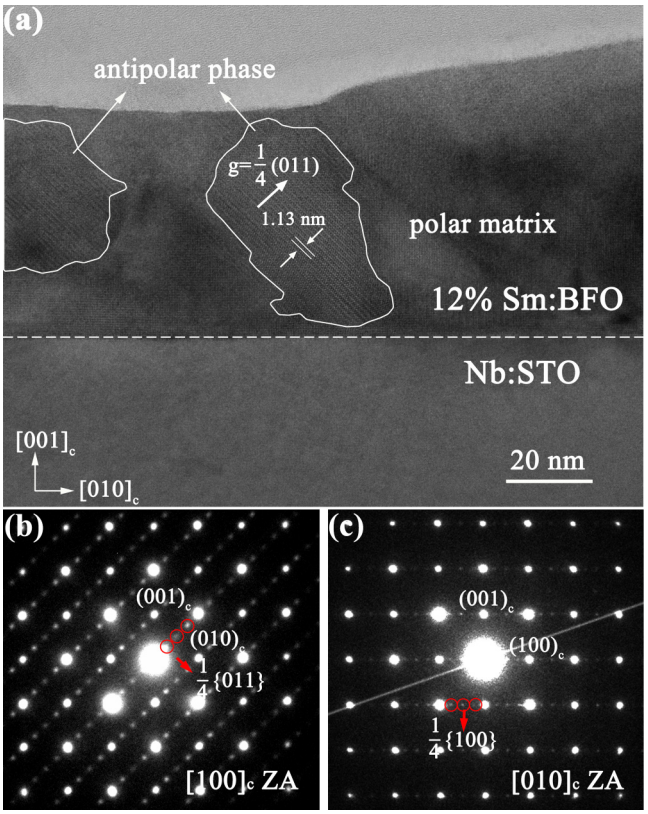

FIG. 2. Phase distribution in the BSFO12 sample. (a) A bright-field TEM image of as-grown BSFO12 thin film, where nanoscale regions of the antipolar phase are marked by white curves. (b) Selected area electron-diffraction pattern viewed along the $[100]_c$ zone axis showing additional $\frac{1}{4}\{011\}$ superlattice reflections. (c) Selected area electron-diffraction pattern viewed along the $[010]_c$ zone axis shows additional $\frac{1}{4}\{100\}$ superlattice reflections. These additional superlattice reflections indicate an antipolar phase with symmetry Pnam.

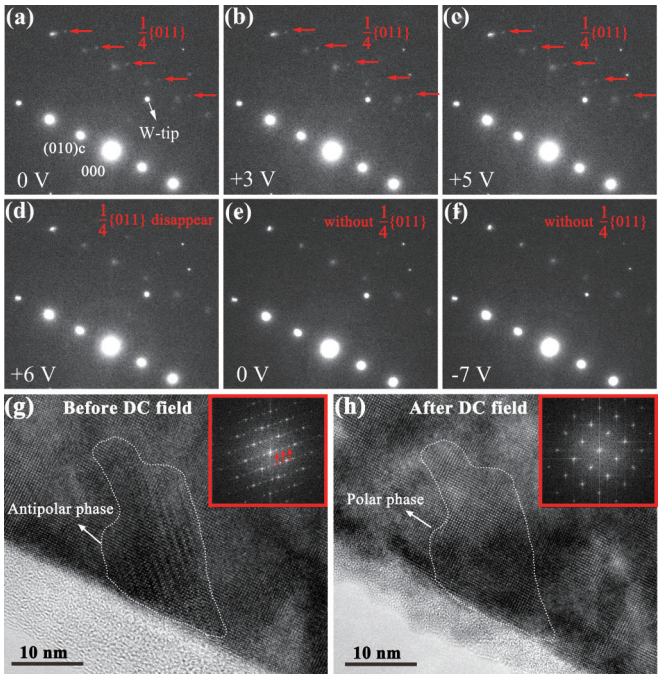

FIG. 3. Phase evolution in the BSFO12 sample. (a)–(f) snapshots of selected diffraction pattern evolution during the process of applying external dc electric bias in the following order: $0 \rightarrow +7 \rightarrow 0 \rightarrow -7$ V, showing the disappearance of $\frac{1}{4}\{011\}$ superstructure reflections at a bias of +6 V, where the superstructure reflections are indicated by red arrows in (a)–(f). The $\frac{1}{4}\{011\}$ superstructure does not reoccur when applying negative electric bias. (g) and (h) The corresponding high-resolution images before and after applying electric field, showing a clear phase transition from the antipolar phase to the polar phase. The insets in (g) and (h) show the FFT of the region marked by a dashed line, respectively, where distinct structural characterization can be observed.

superlattice reflections, indicating that the lattice parameters of the unit cell are $\sqrt{2}a_c \times 2\sqrt{2}a_c \times 4a_c$ rather than $\sqrt{2}a_c \times 2\sqrt{2}a_c \times 2a_c$ by x-ray diffraction in previous reports [17] (a_c denotes the pseudocubic lattice parameter). According to these features of diffraction patterns, these regions are confirmed to possess an orthorhombic *Pnam* structure (space group no. 62). It is characterized by combining $PbZrO_3$-like antipolar A-site cation displacements along $[110]_c$ direction with complex $(a^-a^-c^+)/(a^-a^-c^-)$ octahedral tilting [24,25]. Here, we denote this phase as an antipolar phase. Such a phase has also been revealed in other rare-earth element doped BFO systems like La:BFO [24] and Nd:BFO [26]. For the BSFO12 thin film, tens of nanometers antipolar $PbZrO_3$-like phases are embedded in the polar rhombohedral matrix, which is in good agreement with the previous studies [10,13].

B. Phase evolution in the BSFO12 sample (pre-MPB)

Phase transition is induced by an applied electric field oriented along the film normal between a surface electric probe and a planar bottom electrode, and the geometry is depicted schematically in Fig. S1 of Ref. [19], which is also used for polarization switching experiment in previous reports [27]. Electron-diffraction patterns of the sample BSFO12 were recorded in real time during the process of applying an external electric field [as shown in Figs. 3(a)–3(f)]. As shown in these figures, $\frac{1}{4}\{011\}$ superlattice reflections marked by red arrows suddenly disappeared at the bias of +6 V. The whole diffraction pattern turned into the simple diffraction pattern of the *R3c* phase. Based on the results of electron-diffraction simulations [19], this phenomenon indicates that the electric field induces a phase transition from the antipolar phase to the polar phase. What is more, no signature of the reappearance of the antipolar phase can be detected during the process of applying negative bias [as shown in Figs. 3(e)–3(f)]. This indicates that the phase transition here is irreversible.

Combining the high resolution electron microscopy (HREM) data with fast Fourier-transform (FFT) results, the irreversible phase transition was further confirmed. Figure 3(g) shows a HREM image along the $[100]_c$ direction before applying electric fields, where a 20-nm region shows a typical $\frac{1}{4}\{011\}$ structural modulation of antipolar phase. After applying electric bias, the sample is tilted to the zone axis to gain a HREM image shown in Fig. 3(h), where the $\frac{1}{4}\{011\}$ structural characterization vanished in both the image and FFT. Therefore, it is reasonable to conclude that the

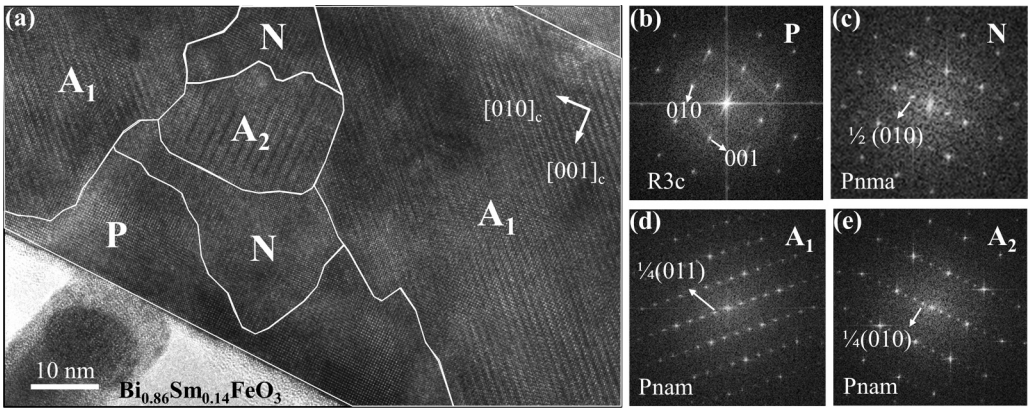

FIG. 4. Phase distribution in the BSFO14 sample. (a) The high-resolution electron microscopy image of 14 at. % Sm-doped BFO thin film, where three phases with distinct structural modulations coexist. (b) The FFT of region P shows fundamental reflections. (c) The FFT of region N shows $\frac{1}{2}\{010\}$ superlattice reflections as an indication of *Pnma* symmetry. (d) and (e) the FFTs of regions A_1 and A_2 show $\frac{1}{4}\{011\}$ and $\frac{1}{4}\{100\}$ superlattice reflections as indications of the *Pnam* symmetry, respectively.

electric field could induce an irreversible phase transition from an antipolar *Pnam* phase to a polar *R3c* phase in BSFO12.

C. Phase distribution in the BSFO14 sample (MPB)

As the doping content of Sm increases to 14 at. %, which is considered as the MPB composition, the phase distribution becomes more complex. Figure 4(a) shows a cross-section HREM image of a BSFO14 thin film, where several mosaic domains with characteristic structural modulations are outlined by white curves. FFT analysis was carried out at the four representative domains in the image, as shown in Figs. 4(b)–4(e). At the top of the thin film (region P), the square-shaped lattice resembles that of parent BFO, and the corresponding FFT pattern [Fig. 4(b)] has only fundamental reflections of parent BFO *R3c* phase. Thus, region P is confirmed to be the polar ferroelectric phase. At the central part of the thin film, there are two regions (region N) with cell-doubled orthorhombic phase which gives rise to $\frac{1}{2}\{010\}$ superlattice reflections in addition to fundamental reflections in FFT pattern as shown in Fig. 4(c). This phase possesses *Pnma* space-group symmetry (space group no. 62) with the $a^-a^-c^+$ tilt pattern [28], which is recognized as a nonpolar phase [10]. There are other regions in this image (region A_1 and A_2) characterized by $\frac{1}{4}\{011\}$ and $\frac{1}{4}\{100\}$ superlattice reflections, respectively, in the FFT patterns as shown in Figs. 4(d) and 4(e), which are indications of antipolar phase discussed above. All these results are in agreement with other studies [10,13,18].

D. Phase evolution in the BSFO14 sample (MPB)

Figure 5 shows the snapshots of the phase evolution in 14 at. % Sm-doped BFO during the switch of external electric field in our *in situ* experiment. It is worth noting that each image in Fig. 5 is a HREM image (refer to the movie in Ref. [19] for larger images), so that we can distinguish clearly each phase by lattice structure modulation and FFT. Figure 5(a) demonstrates that three phases coexist at the onset of the *in situ* experiment, the same as Fig. 4(a). Such distribution did not change until the bias decreased to −4 V [Fig. 5(b)]. At −4 V, polar phase at the top interface with negative bias began to grow forward rapidly with the decrease in the bias [Figs. 5(c) and 5(d)]. At the bias of −7 V, major field of view turned into the polar phase and the phase distribution became stable [Fig. 5(e)]. Nonpolar phase began to nucleate when the applied bias increased to 0 V and grew with the increase of bias at the range of 0 to 2 V [Figs. 5(f)–5(h)]. Then these two phases began to diminish again when the bias increased further, and the whole field of view in the image turns into polar phase at 6 V [Figs. 5(i) and 5(j)]. The whole field of view kept as the polar state until the bias decreased to 0 V [Fig. 5(k)]. Nonpolar phase and antipolar phase nucleated again when the bias decreased to −1 V [Fig. 5(l)]. Our observation shows a reversible phase transition between the polar phase and the nonpolar/antipolar phase. A higher voltage makes the polar phase more stable. The voltage leading a transition from nonpolar/antipolar phase to polar phase is around ±3 V, and it is around ±1 V for the reversal process.

In our observations, the newly formed polar phase was stable even after the removal of applied voltage in the pre-MPB sample, whereas in the MPB sample the phase transition between the antipolar/nonpolar phase and the polar phase is reversible. Thermodynamic calculation based on the Ginzburg-Landau-Devonshire theory [29] was carried out to rationalize our observations. Figures 6(a) and 6(b) show the Landau free-energy landscape as a function of ferroelectric polarization P_1 and P_2 in the sample with 12- and 14 at. % Sm doping respectively, where P_3 and the antiferroelectric order parameter are optimized to minimize the free energy (see method section for details). The minima at $P = 0$ denotes the antipolar phase, and the other four minima indicate the polar phase. The free energies of both polar and antipolar phases increase and the energy barrier of the phase transition between polar and antipolar phases decreases with increasing Sm-doping content, as shown in Fig. 6(c). Therefore, for 12 at. % Sm composition, the thermal fluctuation cannot overcome the energy barrier, giving rise to an irreversible phase transition, whereas for 14 at. % Sm composition, the smaller energy barrier can be overcome

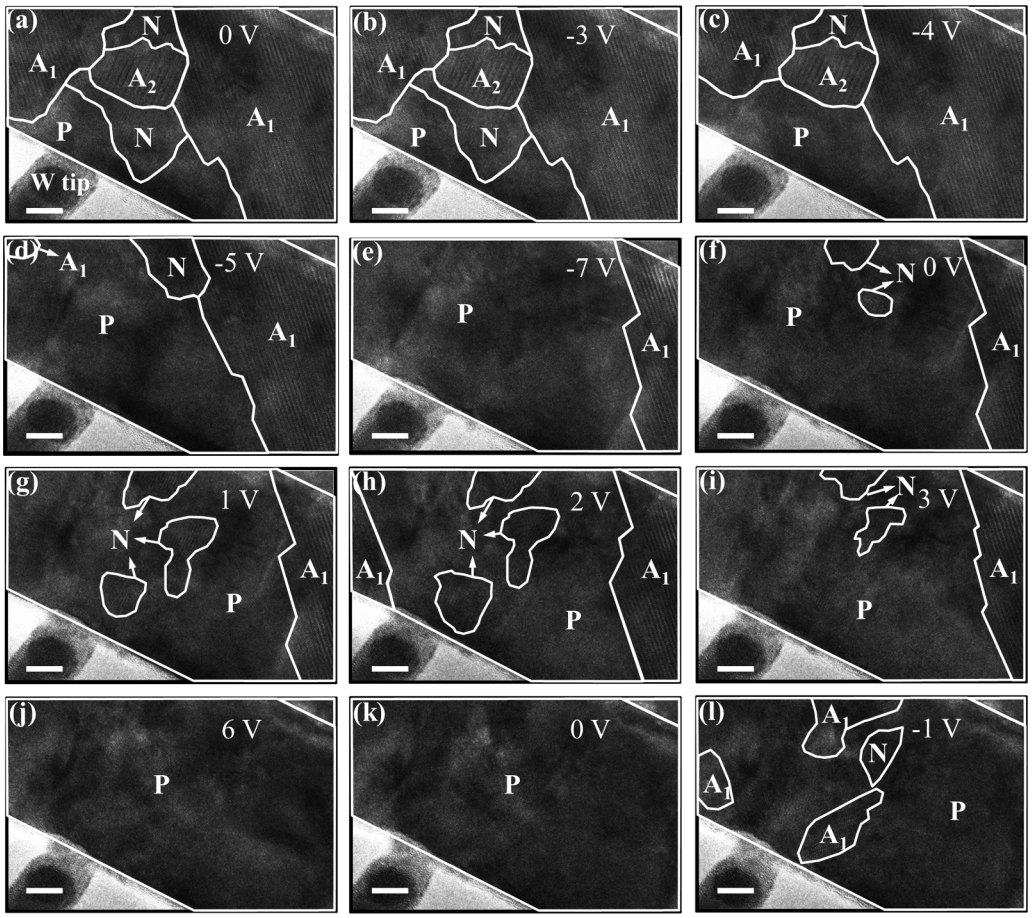

FIG. 5. Phase evolution in the BSFO14 sample. A chronological HREM image series demonstrates the phase evolution of three phases under the switch of an external electric field ($0 \rightarrow -7 \rightarrow 0 \rightarrow +7 \rightarrow -1$ V). The scale bar represents 10 nm. Different phases are marked by white curves and capital letters: P denotes polar phase; N denotes nonpolar phase; A_1 and A_2 denote antipolar phase with two different zone axes. (a) The same image shown in Fig. 4(a) demonstrates the starting point of the *in situ* experiment. (b) HREM image at -3 V with no difference from (a). (c)–(e) Polar phase is growing and nonpolar phase and antipolar phase are diminishing with the decrease of applied bias from -4 to -7 V. (f) Nonpolar phase begins to nucleate when applied bias increases to 0 V. (g) and (h) Nonpolar phase and antipolar phase are growing with increase of the bias from 0 to 2 V. (i) Nonpolar phase and polar phase begin to diminish when the bias increases. (j) The whole field of view in the image turns into polar phase at 6 V. (k) The whole field of view keeps the polar state until the bias decrease to 0 V. (l) Nonpolar phase and antipolar phase begin to nucleate at -1 V.

by the thermal fluctuation, leading to a reversible phase transition.

An interesting macroscopic observation in the Sm-doped BFO system is the double hysteresis P-E loop near the MPB [9,12]. Our microscopic observation of phase transition provides a direct interpretation for the origin of this phenomenon. Following our experimental results by *in situ* electron microscopy, the P-E loop should be broken into several processes as shown in Fig. 7: A high electric field (800 kV/cm) favoring the polar phase over the antipolar/nonpolar phase will lead to an abrupt increase of the polarization (process I). The polar phase is stable at the beginning of the switching process, leading to little change in polarization (process II). Then, a relative low negative electric field ~ -200 kV/cm will drive the nucleation and growth of the antipolar/nonpolar phase, leading to an abrupt decrease of the polarization (process III). A higher negative electric field ~600 kV/cm will stimulate the opposite process to form the polar phase with negative polarization (process IV). The negative polar phase maintains stable until a low positive bias is applied (process V). Then, the macroscopic polarization decreases abruptly with the phase transition from the polar phase to the antipolar/nonpolar phase under an electric field of 200 kV/cm (process VI). Thus, the origin of the double hysteresis loop observed in the macroscopic measurement can be interpreted using the phase transition model.

The relationship between the strain, electric field, and the piezoelectric response amplitude of the films is described by

$$d_{33} = \frac{\varepsilon_{33}}{E}, \tag{2}$$

where d_{33} is the effective piezoelectric coefficient, and ε_{33} is the strain induced by the electric field E. According to our experimental value of the average bias $U \sim 3V$ for phase transitions and the average thickness $d \sim 51.0$ nm of BSFO14 thin film, the electric field E is estimated as $\sim 5.9 \times 10^2$ kV/cm by $E = U/d$. Combining with the strain induced by phase transition (~1% [18,30]), we therefore

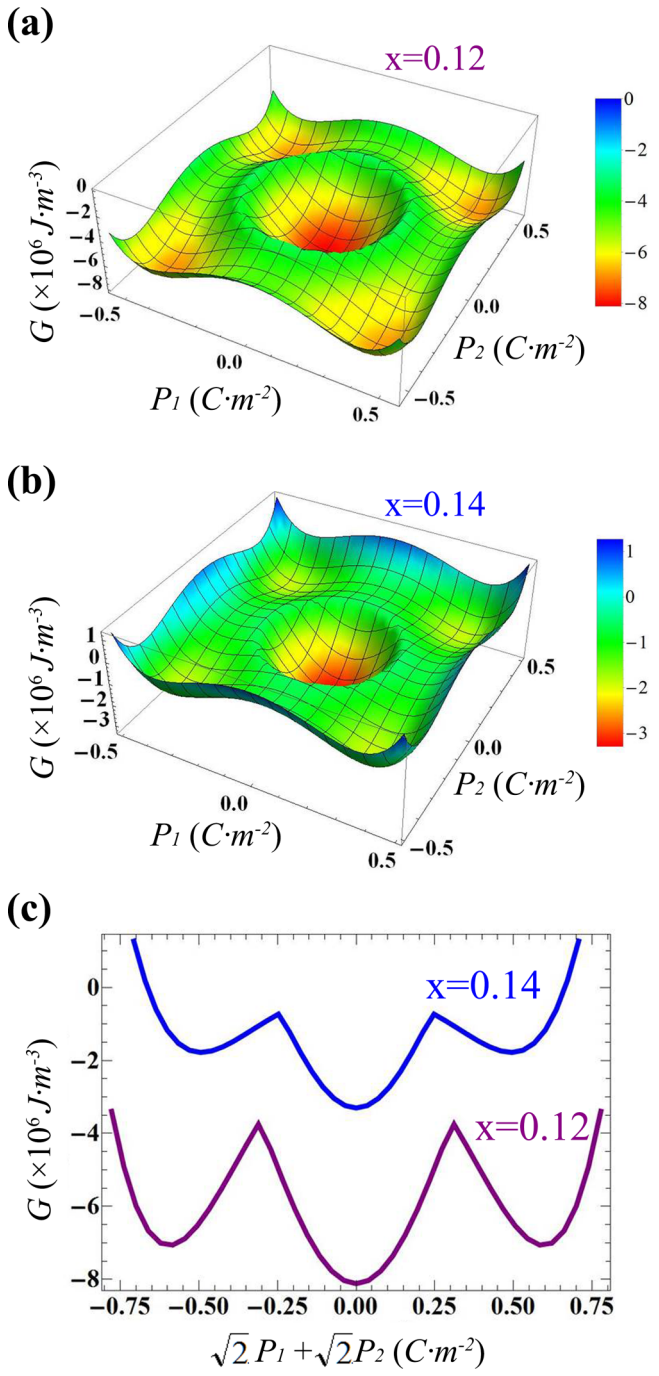

FIG. 6. Phenomenological modeling. (a) and (b) The free-energy density landscape as a function of ferroelectric polarization P_1 and P_2 in the sample BSFO12 and BSFO14, respectively. (c) The energy profile along the $P_1 = P_1$ cross section of (a) and (b).

can estimate that d_{33} due to the phase transition is approximately 170 pm/V, which is in good agreement with the macroscopic measurement by piezoresponse force microscopy (∼110 pm/V [9]). Thus, the enhanced piezoelectric response

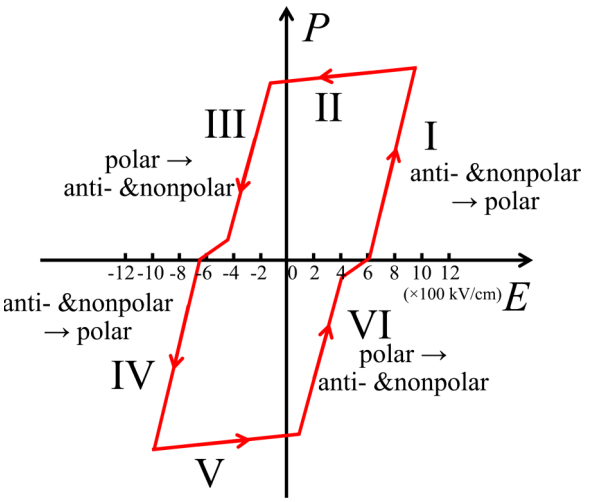

FIG. 7. The sketch of the P-E loop by phase transition model, where the values of electric field E were estimated according to the *in situ* experiments.

is mainly attributed to the phase transition between the polar phase and the antipolar/nonpolar phase in rare-earth element doped BFO with the composition near the MPB.

IV. CONCLUSIONS

In summary, our *in situ* TEM observations with subnanometer resolution clearly show an irreversible phase transition from the antipolar phase to the polar phase in the typical Sm-doped BFO system with the pre-MPB composition and a reversible phase transition between the polar phase and the antipolar/nonpolar phase in the MPB composition. Combined with the phenomenological theory calculation, the origins of double PE hysteresis loop and enhanced piezoelectric response are attributed to the electric-field induced reversible phase transition at the MPB region. The reversible phase transition mechanism proposed here provides a deep understanding of the enhanced electromechanical response for the rare-earth element doped BFO system with the composition near the MPB.

ACKNOWLEDGMENTS

We thank Dr. Lin Xie and Dr. Jiamian Hu for helpful discussions. This paper was financially supported by Chinese National Natural Science Foundation (Grants No. 11374174, No. 51390471, and No. 51527803), National 973 Project of China (Grant No. 2015CB654902), and National Key Research and Development program (Grant No. 2016YFB0700402). This paper made use of the resources of the National Center for Electron Microscopy in Beijing and Tsinghua National Laboratory for Information Science and Technology. The work at The Pennsylvania State University is supported by the U.S. Department of Energy, Office of Basic Energy Sciences, Division of Materials Sciences and Engineering under Award No. FG02-07ER46417 (F.X. and L.-Q.C.).

[1] S.-E. Park and T. R. Shrout, J. Appl. Phys. **82**, 1804 (1997).

[2] R. Guo, L. E. Cross, S.-E. Park, B. Noheda, D. E. Cox, and G. Shirane, Phys. Rev. Lett. **84**, 5423 (2000).

[3] R. E. Cohen and H. Fu, Nature (London) **403**, 281 (2000).
[4] H. Wang, J. Zhu, N. Lu, A. A. Bokov, Z.-G. Ye, and X. W. Zhang, Appl. Phys. Lett. **89**, 42908 (2006).
[5] Y. Saito, H. Takao, T. Tani, T. Nonoyama, K. Takatori, T. Homma, T. Nagaya, and M. Nakamura, Nature (London) **432**, 84 (2004).
[6] E. Cross, Nucl. Med. Commun. **32**, 666 (2011).
[7] J. Wang, J. B. Neaton, H. Zheng, V. Nagarajan, S. B. Ogale, B. Liu, D. Viehland, V. Vaithyanathan, D. G. Schlom, U. V. Waghmare, N. A. Spaldin, K. M. Rabe, M. Wuttig, and R. Ramesh, Science **299**, 1719 (2003).
[8] R. J. Zeches, M. D. Rossell, J. X. Zhang, A. J. Hatt, Q. He, C.-H. Yang, A. Kumar, C.H. Wang, A. Melville, C. Adamo, G. Sheng, Y.-H. Chu, J. F. Ihlefeld, R. Erni, C. Ederer, V. Gopalan, L.-Q. Chen, D. G. Schlom, N. A. Spaldin, L. W. Martin, and R. Ramesh, Science **326**, 977 (2009).
[9] S. Fujino, M. Murakami, V. Anbusathaiah, S. H. Lim, V. Nagarajan, C. J. Fennie, M. Wuttig, L. Salamanca-Riba, and I. Takeuchi, Appl. Phys. Lett. **92**, 202904 (2008).
[10] C. J. Cheng, D. Kan, S. H. Lim, W. R. McKenzie, P. R. Munroe, L. G. Salamanca-Riba, R. L. Withers, I. Takeuchi, and V. Nagarajan, Phys. Rev. B **80**, 014109 (2009).
[11] D. Kan, V. Anbusathaiah, and I. Takeuchi, Adv. Mater. **23**, 1765 (2011).
[12] D. Kan, L. Pálová, V. Anbusathaiah, C. J. Cheng, S. Fujino, V. Nagarajan, K. M. Rabe, and I. Takeuchi, Adv. Funct. Mater. **20**, 1108 (2010).
[13] C.-J. Cheng, A. Y. Borisevich, D. Kan, I. Takeuchi, and V. Nagarajan, Chem. Mater. **22**, 2588 (2010).
[14] W. Sun, J.-F. Li, Q. Yu, and L.-Q. Cheng, J. Mater. Chem. C **3**, 2115 (2015).
[15] W. Sun, J.-F. Li, F. Zhu, Q. Yu, L.-Q. Cheng, and Z. Zhou, Phys. Chem. Chem. Phys. **17**, 19759 (2015).
[16] C. A. Wang, H. Z. Pang, A. H. Zhang, M. H. Qin, X. B. Lu, X. S. Gao, M. Zeng, and J.-M. Liu, J. Phys. D **48**, 395302 (2015).
[17] J. Walker, H. Ursic, A. Bencan, B. Malic, H. Simons, I. Reaney, G. Viola, V. Nagarajan, and T. Rojac, J. Mater. Chem. C **4**, 7859 (2016).
[18] A. Y. Borisevich, E. A. Eliseev, A. N. Morozovska, C.-J. Cheng, J.-Y. Lin, Y. H. Chu, D. Kan, I. Takeuchi, V. Nagarajan, and S. V. Kalinin, Nat. Commun. **3**, 775 (2012).
[19] See Supplemental Material at http://link.aps.org/supplemental/10.1103/PhysRevB.95.214101 for details of the material synthesis method, the schematic image of *in situ* TEM setup, the results of electron-diffraction simulation, and two movies of *in situ* experiments with sample 12 and 14 at. % Sm doped BFO, respectively.
[20] F. Xue, L. Liang, Y. Gu, I. Takeuchi, S. V. Kalinin, and L.-Q. Chen, Appl. Phys. Lett. **106**, 12903 (2015).
[21] S. Jesse, A. P. Baddorf, and S. V. Kalinin, Appl. Phys. Lett. **88**, 62908 (2006).
[22] S. Jesse, H. N. Lee, and S. V. Kalinin, Rev. Sci. Instrum. **77**, 73702 (2006).
[23] W. Sun, Q. Yu, J. Li, and J.-F. Li, J. Phys. Chem. C **119**, 19891 (2015).
[24] V. A. Khomchenko, I. O. Troyanchuk, D. V. Karpinsky, S. Das, V. S. Amaral, M. Tovar, V. Sikolenko, and J. A. Paixão, J. Appl. Phys. **112**, 84102 (2012).
[25] I. O. Troyanchuk, D. V. Karpinsky, M. V. Bushinsky, V. A. Khomchenko, G. N. Kakazei, J. P. Araujo, M. Tovar, V. Sikolenko, V. Efimov, and A. L. Kholkin, Phys. Rev. B **83**, 054109 (2011).
[26] I. Levin, S. Karimi, V. Provenzano, C. L. Dennis, H. Wu, T. P. Comyn, T. J. Stevenson, R. I. Smith, and I. M. Reaney, Phys. Rev. B **81**, 020103 (2010).
[27] C. T. Nelson, P. Gao, J. R. Jokisaari, C. Heikes, C. Adamo, A. Melville, S.-H. Baek, C. M. Folkman, B. Winchester, Y. Gu, Y. Liu, K. Zhang, E. Wang, J. Li, L.-Q. Chen, C.-B. Eom, D. G. Schlom, and X. Pan, Science **334**, 968 (2011).
[28] A. M. Glazer, Acta Crystallogr. Sect. B **28**, 3384 (1972).
[29] A. F. Devonshire, Adv. Phys. **3**, 85 (1954).
[30] M. Kubota, K. Oka, Y. Nakamura, H. Yabuta, K. Miura, Y. Shimakawa, and M. Azuma, Jpn. J. Appl. Phys. **50**, 09NE08 (2011).